Ultrasmall [^{64}Cu]Cu Nanoclusters for Targeting Orthotopic Lung Tumors Using Accurate Positron Emission Tomography Imaging

Fuping Gao,[†,§] Pengju Cai,[‡,§] Wenjiang Yang,[¶] Jingquan Xue,[¶] Liang Gao,[†] Ru Liu,[†] Yaling Wang,[†] Yawei Zhao,[⊥] Xiao He,[†] Lina Zhao,[†] Guodong Huang,[‡] Fasheng Wu,[‡] Yuliang Zhao,[†] Zhifang Chai,[†] and Xueyun Gao*[,†]

[†]CAS Key Laboratory for Biological Effects of Nanomaterials and Nanosafety and [¶]CAS Key Laboratory of Nuclear Radiation and Nuclear Energy Technology, Institute of High Energy Physics, Chinese Academy of Sciences, Beijing 100049, People's Republic of China, [‡]Affiliated Ruikang Hospital of Guangxi University of TCM, Nanning, Guangxi 530011, People's Republic of China, and [⊥]School of Physics, Beijing Institute of Technology, Beijing 100081, People's Republic of China. [§]F. Gao and P. Cai contributed equally to this work.

ABSTRACT Positron emission tomography (PET) imaging has received special attention owing to its higher sensitivity, temporal resolution, and unlimited tissue penetration. The development of tracers that target specific molecules is therefore essential for the development and utility of clinically relevant PET procedures. However, ^{64}Cu as a PET imaging agent generally has been introduced into biomaterials through macrocyclic chelators, which may lead to the misinterpretation of PET imaging results due to the detachment and transchelation of ^{64}Cu. In this study, we have developed ultrasmall chelator-free radioactive [^{64}Cu]Cu nanoclusters using bovine serum albumin (BSA) as a scaffold for PET imaging in an orthotopic lung cancer model. We preconjugated the tumor target peptide luteinizing hormone releasing hormone (LHRH) to BSA molecules to prepare [^{64}Cu]Cu_{NC}@BSA-LHRH. The prepared [^{64}Cu]Cu nanoclusters showed high radiolabeling stability, ultrasmall size, and rapid deposition and diffusion into tumor, as well as predominantly renal clearance. [^{64}Cu]Cu_{NC}@BSA-LHRH showed 4 times higher tumor uptake compared with that of [^{64}Cu]Cu_{NC}@BSA by analyzing the ^{64}Cu radioactivity of tissues *via* gamma counting. The PET imaging using [^{64}Cu]Cu nanoclusters as tracers showed more sensitive, accurate, and deep penetration imaging of orthotopic lung cancer *in vivo* compared with near-infrared fluorescence imaging. The nanoclusters provide biomedical research tools for PET molecular imaging.

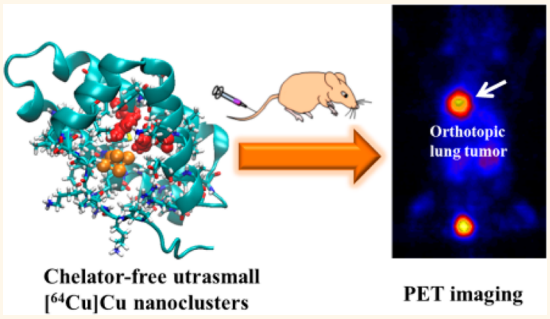

KEYWORDS: ^{64}copper nanoclusters · positron emission tomography imaging · orthotopic lung tumor · tumor target · luteinizing hormone releasing hormone

Positron emission tomography (PET) imaging has become widely used as a diagnostic imaging tool owing to their higher detection sensitivity (down to the picomolar level), approximately 10^6 times higher than magnetic resonance imaging (MRI), high temporal resolution, unlimited tissue penetration, and ability to conduct quantitative analysis of whole-body images.[1−4] Copper-based radionuclides are currently being extensively evaluated. The half-life (12.7 h) and decay properties (β^+, 0.653 MeV, 17.8%; β^-, 0.579 MeV, 38.4%; the remainder is electron capture) of ^{64}Cu make it an ideal radioisotope for PET imaging and targeted radiotherapy for cancer.[5]

Generally, ^{64}Cu have been introduced into various nanoparticles (NPs), such as quantum dots,[6,7] gold NPs,[8,9] carbon nanomaterials,[10] and polymeric NPs,[11−13] peptides,[14] and proteins through macrocyclic chelators such as 1,4,7,10-tetraazacyclododecane-1,4,7,10-tetraacetic acid (DOTA, stability constants, K_{ML} = 22.2) or 1,4,8,11-tetraazacyclododecane-1,4,8,11-tetraacetic acid (TETA, stability constants, K_{ML} = 21.1)[15,16] to form stable complexes for noninvasive *in vivo* nuclear imaging. However, there are two inherent limitations associated with the use of

* Address correspondence to gaoxy@ihep.ac.cn.

Received for review December 15, 2014 and accepted April 28, 2015.

Published online April 28, 2015
10.1021/nn507130k

radiometal−chelator complexes for nuclear imaging and *in vivo* study.[17] First, radiometal−chelator complexes have poor *in vivo* stability. These conventional bifunctional chelators such as TETA or DOTA can bind many different metal ions, which leads to the release of some copper. In addition, a number of compounds result in a reduction of Cu(II) to Cu(I) *in vivo* and subsequent loss of the Cu, which can then be complexed by proteins in both the blood and liver such as superoxide dismutase (SOD) and result in high accumulation of Cu in the liver.[18] Although ^{64}Cu-TETA complexes are more stable than ^{64}Cu-DOTA, their instability *in vivo* has been well documented. Bass *et al.* demonstrated that when ^{64}Cu-TETA-octreotide (OC) was injected into normal Sprague−Dawley rats, nearly 70% of the ^{64}Cu from ^{64}Cu-TETA-OC was transchelated to a 35 kDa species believed to be superoxide dismutase in the liver 20 h postinjection.[18] Second, the physicochemical properties of NPs may be influenced by attaching radiometal−chelator complexes to their surface. The two factors may lead to the misinterpretation of PET imaging result.[19,20] To address these concerns, many radiolabeling strategies have been developed, including ^{64}Cu-loaded liposomes,[21] the chelator-free strategy of using ^{64}Cu-porphysomes,[22,23] and direct incorporation of ^{64}Cu into nanomaterials.[24−26] However, the higher particle size of these nanomaterials causes significantly higher liver accumulation and slow clearance properties *in vivo*.

Recently, metal nanoclusters have attracted considerable attention because of their unique properties that differ substantially from those of the corresponding atoms and bulk materials. Owing to their ultrasmall size, good biocompatibility, high stability, robust preparation, and luminescent properties,[27,28] metal nanoclusters exhibit great potential as emerging functional materials for a variety of biomedical applications.

In the current study, we synthesized radioactive [^{64}Cu]Cu nanoclusters (NCs) ([^{64}Cu]Cu$_{NC}$@BSA) by a simple one-pot chemical reduction method by using bovine serum albumin (BSA) as template or scaffold, in which ^{64}Cu is an integral building block of Cu$_{NC}$@BSA rather than chelated to the nanoclusters. [^{64}Cu]Cu$_{NC}$@BSA provides significant advantages for PET imaging including (1) the greatly improved radiolabeling stability ensures diagnostic accuracy; (2) the ultrasmall size and the peptide shell give [^{64}Cu]Cu$_{NC}$@BSA superior features such as the ability to easily escape the reticuloendothelial system (RES), thus improving their deposition in tumor, rapid diffusion, and predominantly renal clearance;[29] (3) the BSA shell can be conjugated to other functional molecules without effects from macrocyclic chelators. In the study, we preconjugated luteinizing hormone releasing hormone (LHRH) peptide to BSA molecules to prepare [^{64}Cu]Cu$_{NC}$@BSA-LHRH. The LHRH peptide acts as a targeting moiety,[30−32] whose receptors are overexpressed in several types of cancer cells, such as breast, ovarian, prostate, lung, and hepatic cancer cells. We demonstrate [^{64}Cu]Cu$_{NC}$@BSA-LHRH as a tumor PET imaging agent for early, sensitive, and accurate diagnosis in a primary (orthotopic) lung cancer model. To the best of our knowledge, this is the first report on the use of chelator-free nanoclusters for orthotopic lung cancer PET imaging.

RESULTS

Synthesis, Characterization, and Stability. We began the synthesis of nanoclusters with nonradioactive copper chloride ($CuCl_2$) using BSA as template (Cu$_{NC}$@BSA). For the synthesis of Cu$_{NC}$@BSA-LHRH, LHRH peptide was preconjugated to BSA molecules, and then the nanoclusters were synthesized using BSA-LHRH conjugates as template. The conjugation numbers for LHRH were quantified by matrix-assisted laser desorption ionization time-of-flight (MALDI-TOF). The high-resolution transmission electron microscope (HRTEM) images showed Cu$_{NC}$@BSA were ultrasmall and well-dispersed with an average diameter of 3 nm (Figure 1a). The HRTEM of Cu$_{NC}$@BSA-LHRH showed no significant change compared with that of Cu$_{NC}$@BSA (Figure S1). The hydrodynamic sizes of the Cu$_{NC}$@BSA were determined using dynamic light scattering (DLS) (Figure 1b). The Cu$_{NC}$@BSA showed a DLS size of 3.5 $\pm$ 0.5 nm. The Cu$_{NC}$@BSA-LHRH showed a slightly increased DLS size of 3.8 $\pm$ 0.5 nm (Figure S1). The zeta potential of the Cu$_{NC}$@BSA was −17.1 mV, attributed to the negative charge of the BSA shell. The Cu$_{NC}$@BSA-LHRH displayed a slightly changed zeta potential of −15.8 mV. Figure 1c presents UV−vis absorption and emission spectra of BSA (black line), Cu$_{NC}$@BSA (red line), and Cu$_{NC}$@BSA-LHRH solution (blue line). Pure BSA shows strong absorption at 280 nm. Compared with the absorption spectra of BSA, Cu$_{NC}$@BSA and Cu$_{NC}$@BSA-LHRH present weaker absorption at 280 nm. This indicated the formation of a new type of material in the protein environment. The conjugation of LHRH in the BSA complex did not significantly affect the UV−vis absorption. In addition, once Cu nanoclusters formed, it will present luminescence characteristics. Cu$_{NC}$@BSA and Cu$_{NC}$@BSA-LHRH show a lavender color under visible light (I, II) and blue fluorescence under UV light (III, IV) (Figure S2). Both Cu$_{NC}$@BSA and Cu$_{NC}$@BSA-LHRH have a photoluminescence (PL) peak at ~410 nm. However, BSA itself virtually has no emission peak at 410 nm (Figure 1c). As-synthesized material has been studied by MALDI-TOF mass spectrometry (MS) to understand the number of copper atoms in the cluster core. The mass spectrum of BSA showed two peaks at around 66 400 Da and 33 200 Da due to the monocation and bication (Figure 1d), which agrees with previous results.[33] The Cu$_{NC}$@BSA showed distinct, but low-intensity peaks at *m/z* 33 357 Da due to the doubly charged ion form. The difference between the above

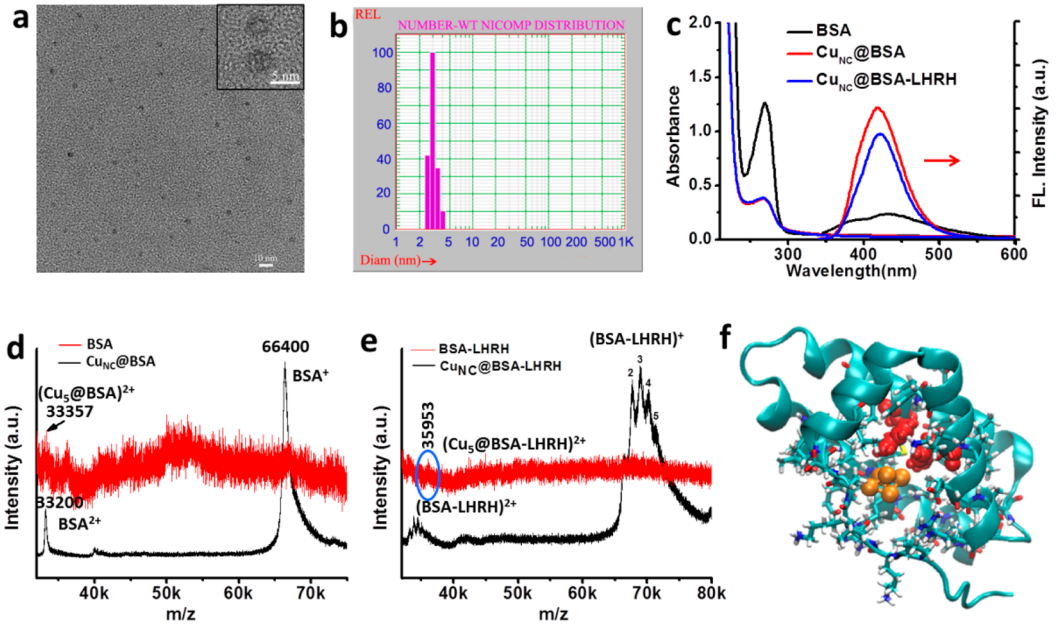

Figure 1. Characterizations of Cu nanoclusters. (a) HRTEM image of Cu_{NC}@BSA. Inset for a high-magnification HRTEM image of Cu_{NC}@BSA. (b) Size distribution of Cu_{NC}@BSA by dynamic light scattering (DLS). (c) UV−vis absorption and emission spectra of BSA (black line), Cu_{NC}@BSA solution (red line), and Cu_{NC}@BSA-LHRH solution (blue line) at room temperature. (d) MALDI-TOF mass spectra of BSA (black) and Cu_{NC}@BSA (red). The black arrow shows doubly charged ions of Cu_{NC}@BSA. (e) MALDI-TOF mass spectra of BSA-LHRH (black) and Cu_{NC}@BSA-LHRH (red). The blue ellipse shows doubly charged ions of Cu_{NC}@BSA-LHRH. The numbers indicate the number of conjugated LHRH peptides. (f) Molecular structure of the binding pocket for Cu_5-I (orange) inside the BSA molecule. Tyr137 and Tyr160 are highlighted in red.

peaks with the host protein spectrum measured may be attributed to the five copper atoms. We assign the constitution of clusters as Cu_5@BSA. The mass spectrum of BSA-LHRH conjugation appeared in the regions of 68 993−72 882 Da and 34 497−36 441 Da due to the monocation and bication, which was attributed to the conjugation of two to five LHRH molecules in the BSA complex. The mass spectrum of Cu_{NC}@BSA-LHRH appeared at around *m/z* 35 953 Da due to the doubly charged ion form, which can be attributed to Cu_5@BSA-$LHRH_4$ (Figure 1e). The presence of doubly charged ion clusters along with the corresponding peaks of the protein observed in the MALDI MS data clearly indicate that the Cu cluster is associated with a single protein molecule (Figure 1d and e). From all the results obtained so far, we conclude that the copper nanoclusters (Cu NCs) are formed within BSA or BSA-LHRH conjugation. All of these characteristics indicated the presence of Cu nanoclusters. The obtained Cu nanoclusters are found to be very stable, and the Cu atoms tightly anchored to BSA or the BSA-LHRH conjugation molecule in Cu NCs. The emission peak remains unchanged when Cu_{NC}@BSA-LHRH is dispersed in physiological saline, fetal bovine serum (FBS), high-glucose Dulbecco's modified Eagle's medium (DMEM) medium, and 1 mM cysteine in phosphate-buffered saline (PBS) after 24 h incubation at room temperature (Figure S3) or acidic pH conditions at pH 6.0 (Figure S4). Cu_{NC}@BSA reveals a similar phenomenon to Cu_{NC}@BSA-LHRH (data not shown).

To better understand the synthesis and stability of Cu_{NC}@BSA, we utilized molecular simulations to figure out the conformation details of the Cu_5 nanocluster anchored in the BSA molecule. The possible configurations of the Cu_5 nanocluster were obtained using density functional theory (DFT) calculations.[34,35] There are two isomers, denoted as Cu_5-I and Cu_5-II, for the Cu_5 nanocluster (Figure S5a and b respectively). We built the conformation of the BSA molecule from its molecular dynamics (MD) relaxation. On the basis of the steric isomerism of the Cu_5 nanocluster, we investigated the binding sites for both Cu_5-I and Cu_5-II into BSA by performing molecular docking simulations. As a result, Cu_5-I and Cu_5-II bind to the same binding pocket in BSA with a similar binding mode. In the following, we took Cu_5-I as the example (Cu_5 nanocluster) to study the binding site and binding mode in the Cu_5@BSA complex (same as Cu_5@BSA-LHRH). The overall view of the Cu_5@BSA complex is depicted in Figure S5c, where the Cu_5 nanocluster is buried inside the binding pocket in domain I (highlighted in cyan) of BSA. We show the Cu_5 nanocluster buried binding pocket in detail in Figure 1f. In the binding pocket, the Cu_5 nanocluster locates on the hydrophilicity/hydrophobicity interface composed of hydrophilic Tyr137, Tyr160, and Arg185 and hydrophobic Ile141, Ile181, and Pro117. Among these residues inside the binding pocket, Tyr137 and Tyr160 with quinonyl (highlighted in red) are able to reduce Cu^{2+} of the $CuCl_2$ solution into Cu atoms and then possibly synthesize the *in situ* grown Cu_5 nanocluster.

The *in situ* grown Cu_5 nanocluster prefers to locate in its "birthplace" stably by contacting the hydrophilicity/hydrophobicity interface from the above molecular docking analysis. As a result, the Cu_5 nanocluster is synthesized by the BSA template and can be stably buried inside the binding pocket in BSA without being exposed to the solution environment, which provides a detailed molecular mechanism for the experimental synthesis and stability results.

We prepared [^{64}Cu]Cu_{NC}@BSA and [^{64}Cu]Cu_{NC}@BSA-LHRH using the same procedures as that of plain Cu_{NC}@BSA and Cu_{NC}@BSA-LHRH. The specific activity was readily controlled by varying the radioactivity of $^{64}CuCl_2$ in the mixture of $^{64}CuCl_2$ and cold $CuCl_2$ at the time of [^{64}Cu]Cu_{NC}@BSA and [^{64}Cu]Cu_{NC}@BSA-LHRH synthesis. Because the $^{64}CuCl_2$ and cold $CuCl_2$ have the same chemical properties, the addition of $^{64}CuCl_2$ will not influence the property of [^{64}Cu]Cu nanoclusters. The radiolabeling efficiency of [^{64}Cu]Cu_{NC}@BSA and [^{64}Cu]Cu_{NC}@BSA-LHRH approached greater than 95% at the end of the synthesis. After incubation in pH 7.4 PBS with a challenging agent of ethylenediaminetetraacetic acid (EDTA, 4 mM)[36] at 37 °C for 24 h, [^{64}Cu]Cu_{NC}@BSA and [^{64}Cu]Cu_{NC}@BSA-LHRH lost a negligible amount of radioactivity; the radiochemical purity still remained at 96.8% and 97.8%, respectively (Figure S6). Furthermore, our serum stability studies showed [^{64}Cu]Cu_{NC}@BSA and [^{64}Cu]Cu_{NC}@BSA-LHRH were stable in FBS without any dissociation or translation of ^{64}Cu at 37 °C for 24 h; the radiochemical purity remained at 98.3% and 95.8%, respectively (Figure S6), which was higher than the 81.5% radiochemical purity of ^{64}Cu-DOTA at 24 h after incubation with serum.[20] The results indicated that [^{64}Cu]Cu nanoclusters have significantly better stability than ^{64}Cu-DOTA and ^{64}Cu was very stably integrated into [^{64}Cu]Cu_{NC}@BSA and [^{64}Cu]Cu_{NC}@BSA-LHRH.

***In Vitro* Lung Tumor Specific Targeting of Cu Nanoclusters.** Before *in vivo* tumor PET imaging, we first evaluated the tumor specificity of the nanoclusters *in vitro*. We utilized the confocal fluorescence microscope to observe the uptake of Cu nanoclusters by human non-small-cell lung cancer A549 cells and noncancerous human embryonic lung fibroblast MRC-5 cells. Immunoblotting analysis verified the expression of LHRH receptors on these cells' membrane (Figure S7). The results are consistent with reports that A549 cells overexpress LHRH receptors and MRC-5 cells lack the LHRH receptor expression on their cell membrane.[37] In order to facilitate intracellular localization, nanoclusters were further conjugated with the near-infrared fluorescent dye CF680R (Figure S8). After incubating 1 mg mL^{-1} CF680R-conjugated Cu_{NC}@BSA and Cu_{NC}@BSA-LHRH with cells for 2 h, the cells were fixed and nuclei stained with SYTOX Green. Cu_{NC}@BSA-LHRH revealed a better cellular uptake than the nontargeted Cu_{NC}@BSA by the A549 cells (Figure 2). The amount of Cu_{NC}@BSA-LHRH taken up by the MRC-5 cells was notably lower than that of the A549 cells. In addition, the amount of cellular uptake of Cu_{NC}@BSA-LHRH by A549 cells decreased with addition of 1 mM free LHRH as a competitive inhibitor of the LHRH receptor. The result corroborates that specific cellular uptake of Cu_{NC}@BSA-LHRH is mainly mediated by LHRH receptors on the surfaces of A549 cells.

The cellular uptake was also quantified by flow cytometry. At the same concentration, the mean fluorescence intensity of A549 cells incubated with Cu_{NC}@BSA-LHRH showed a 2.7 times increase over that with Cu_{NC}@BSA. The addition of 1 mM free LHRH significantly decreased the cellular fluorescence intensity of A549 incubated with Cu_{NC}@BSA-LHRH (Figure 3a). However, MRC-5 cells incubated with Cu_{NC}@BSA-LHRH showed little increase in cellular fluorescence intensity compared with control cells (Figure 3b).

***In Vivo* PET Imaging and Biodistribution.** After confirming the formation of Cu nanoclusters and *in vitro* tumor specific targeting of Cu_{NC}@BSA-LHRH, we selected lung cancer as the platform on which to evaluate [^{64}Cu]Cu_{NC}@BSA and [^{64}Cu]Cu_{NC}@BSA-LHRH *in vivo* PET imaging performance. To determine the optimal dose and duration of PET imaging, we first performed *in vivo* PET imaging in A549 subcutaneous xenografted tumors. Each mouse was injected with about 6.7−7.4 MBq of [^{64}Cu]Cu_{NC}@BSA or [^{64}Cu]Cu_{NC}@BSA-LHRH *via* tail vein, and the tomographic images were acquired on a small-animal PET scanner at various time points postinjection. At 0.5 h postinjection, [^{64}Cu]Cu nanoclusters quickly distributed in various tissues and organs. Except for the strong radioactivity signal from the kidney and bladder of mice within 1 h, which is due to renal clearance of ultrasmall [^{64}Cu]Cu nanoclusters, both the liver and tumor were clearly visualized. The tumor uptake of [^{64}Cu]Cu_{NC}@BSA-LHRH was higher than that of nontargeted [^{64}Cu]Cu_{NC}@BSA (Figure S9). At 4 h postinjection, signals slowly decayed. Therefore, the optimal imaging window was within 4 h postinjection. Quantitative analysis of the biodistribution of [^{64}Cu]Cu nanoclusters was obtained by sacrificing the mice at 4 h postinjection, and the ^{64}Cu radioactivity of tissues *via* gamma counting was analyzed . The kidney showed significant [^{64}Cu]Cu nanocluster accumulation (more than 30% ID/g), which was consistent with *in vivo* PET imaging. The uptake of tumor in mice injected with [^{64}Cu]Cu_{NC}@BSA-LHRH (12% ID/g) was almost 4 times higher than that of mice injected with [^{64}Cu]Cu_{NC}@BSA (3% ID/g). To best mimic localized primary tumor, we used an orthotopic A549 lung tumor model for *in vivo* PET imaging. Both general observation and biopsy illustrated the orthotopic A549 lung tumor was successfully established in the left lung of nude mice (Figure S10). After injecting about 6.7−7.4 MBq of [^{64}Cu]Cu_{NC}@BSA or [^{64}Cu]Cu_{NC}@BSA-LHRH for 0.5 h *via* tail vein into mice bearing orthotopic

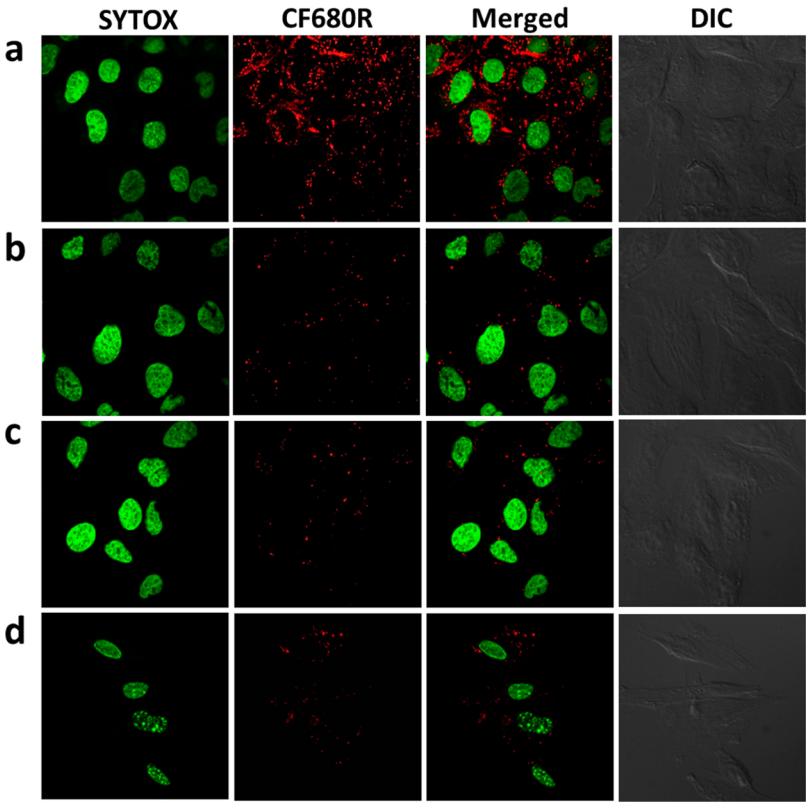

Figure 2. Confocal fluorescence images of *in vitro* cell uptake of Cu nanoclusters. (a) A549 cells cultured with CF680R-conjugated Cu_{NC}@BSA-LHRH for 2 h. (b) A549 cells cultured with CF680R-conjugated Cu_{NC}@BSA for 2 h. (c) A549 cells cultured with CF680R-conjugated Cu_{NC}@BSA-LHRH in the presence of 1 mM free LHRH in the medium after incubation for 2 h. (d) MRC-5 cells cultured with CF680R-conjugated Cu_{NC}@BSA-LHRH for 2 h. Green fluorescence shows nuclear staining with SYTOX green, and red fluorescence shows the internalization of Cu nanoclusters.

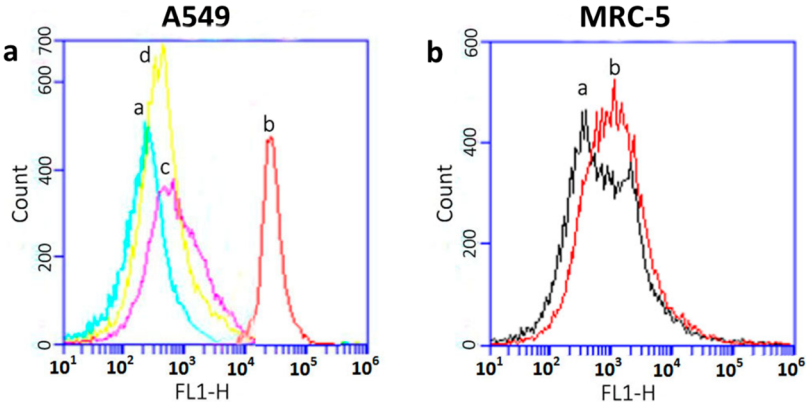

Figure 3. Flow cytometry analysis results of fluorescence signals collected in A549 cells (a) and MRC-5 cells (b) after treatment with Cu nanoclusters for 2 h. (a) Control group cells without any treatment; (b) A549 or MRC-5 cells incubated with CF680R-conjugated Cu_{NC}@BSA-LHRH; (c) A549 cells incubated with CF680R-conjugated Cu_{NC}@BSA-LHRH in the presence of free LHRH peptides as an inhibitor; (d) A549 cells incubated with CF680R-conjugated Cu_{NC}@BSA.

A549 lung tumors, the orthotopic A549 tumors of the left lung were clearly delineated with very little local background in the whole-body PET imaging of mice injected with [^{64}Cu]Cu_{NC}@BSA-LHRH (Figure 4b, videos 5−8 in the Supporting Information). It is noticeable, however, that a significant difference in [^{64}Cu]Cu nanocluster uptake between [^{64}Cu]Cu_{NC}@BSA and [^{64}Cu]Cu_{NC}@BSA-LHRH is observable after 0.5−4 h postinjection. The [^{64}Cu]Cu_{NC}@BSA-LHRH accumulated and was retained preferentially in the orthotopic lung tumor by combined active targeting and passive targeting after injection.[38] Although [^{64}Cu]Cu_{NC}@BSA also showed partial tumor localization due to passive targeting by the effective enhanced permeability and retention (EPR) effect,[38] most of the [^{64}Cu]Cu_{NC}@BSA distributed in the kidney and bladder (Figure 4a, videos 1−4 in the Supporting Information). After the 4 h PET imaging, we sacrificed the mice and collected major

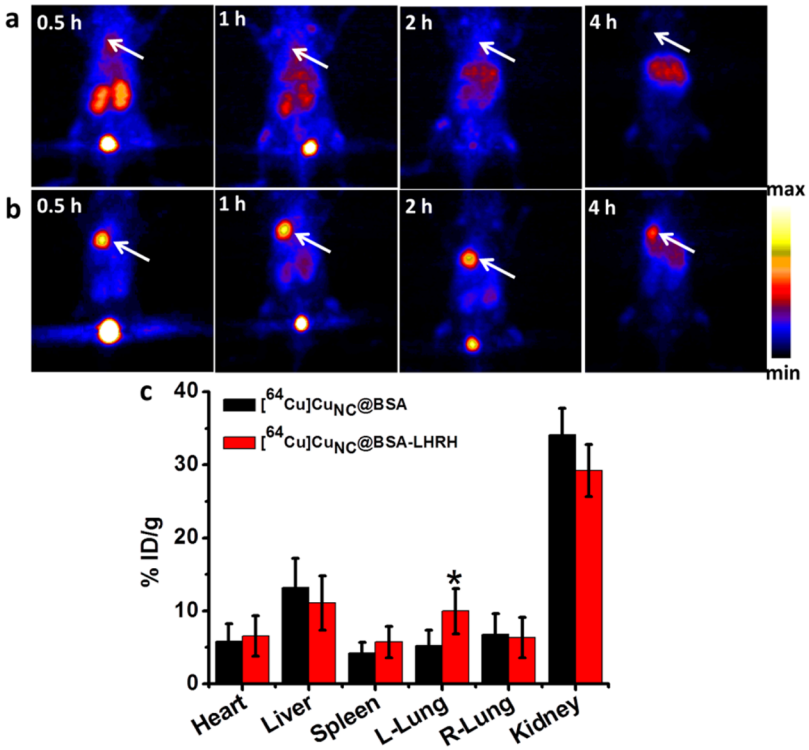

Figure 4. *In vivo* **PET imaging and biodistribution. Representative PET images of coronal single slices on orthotopic A549 lung tumor bearing mice after intravenous injection of 6.7 MBq of [^{64}Cu]Cu$_{NC}$@BSA (a) and [^{64}Cu]Cu$_{NC}$@BSA-LHRH (b). Images were acquired at 0.5, 1, 2, and 4 h. White arrows indicate the lung tumor. Corresponding whole body three-dimensional (3D) PET reconstruction images are shown in supplementary videos 1−4 (after intravenous injection of [^{64}Cu]Cu$_{NC}$@BSA) and videos 5−8 (after intravenous injection of [^{64}Cu]Cu$_{NC}$@BSA-LHRH). (c) Corresponding organ biodistribution of [^{64}Cu]Cu$_{NC}$@BSA and [^{64}Cu]Cu$_{NC}$@BSA-LHRH at 4 h after iv injection in mice bearing orthotopic A549 lung tumor, calculated by γ-counter (n = 3). L-Lung: left lung; R-Lung: right lung. (Asterisk (*) denotes statistical significance. *, $p < 0.05$.)**

organs for analysis of ^{64}Cu radioactivity in different tissues *via* gamma counting. Similar to the results obtained with the mice bearing subcutaneous A549 xenografted tumor, the kidney in mice bearing orthotopic A549 lung tumor shows high radioactivity (about 30% ID/g), which indicates [^{64}Cu]Cu nanoclusters are cleared through the renal route, thus resulting in high accumulation within the kidney and bladder. The radioactivity of the left lung inoculated orthotopic A549 tumor in mice injected with [^{64}Cu]Cu$_{NC}$@BSA-LHRH was 10% ID/g, which was almost 2 times higher than that of mice injected with [^{64}Cu]Cu$_{NC}$@BSA (5.2% ID/g).

As a comparison, we also conducted near-infrared fluorescence (NIRF) imaging in an A549 subcutaneous xenografted tumor model and an A549 orthotopic lung tumor model, respectively, by conjugating near-infrared fluorescent dye CF680R to the decayed [^{64}Cu]Cu nanoclusters. After injecting equivalent doses of nanoclusters with PET imaging into the mice, a similar tumor accumulating profile and biodistribution from average fluorescence signal intensity were also observed with NIRF imaging in the A549 subcutaneous xenografted tumor model (Figure S11). Both *in vivo* imaging and *ex vivo* imaging of excised tumors and major organs showed the CF680R-conjugated [^{64}Cu]Cu$_{NC}$@BSA-LHRH accumulated mainly in the tumor and the kidneys. The CF680R-conjugated [^{64}Cu]Cu$_{NC}$@BSA showed notable localization mainly in the kidneys (Figure S11). However, for the A549 orthotopic lung tumor model, we did not observe a significant fluorescent signal *in vivo* from left lung inoculated orthotopic A549 tumors even after intravenous injection of CF680R-conjugated [^{64}Cu]Cu$_{NC}$@BSA-LHRH (Figure S12a, video 9 in the Supporting Information). However, both *ex vivo* imaging of excised major organs and the biodistribution from average fluorescence signal intensity show left lung inoculated orthotopic A549 tumors have a significant fluorescent signal after intravenous injection of CF680R-conjugated [^{64}Cu]Cu$_{NC}$@BSA-LHRH (Figure S12).

For further verification, we observed the location of the CF680R-conjugated [^{64}Cu]Cu$_{NC}$@BSA and [^{64}Cu]Cu$_{NC}$@BSA-LHRH in the main organs by histological examination of cryosections after 4 h of injection. For the CF680R-conjugated [^{64}Cu]Cu$_{NC}$@BSA-LHRH at 4 h postinjection, the [^{64}Cu]CuNC@BSA-LHRH were mainly located in left lung inoculated orthotopic A549 tumors and kidney, while little fluorescence in the liver and the spleen was noted. There was almost no accumulation in the heart and the right lung (Figure 5). In contrast, the fluorescence in the left lung and right lung from the mouse injected with the CF680R-conjugated [^{64}Cu]Cu$_{NC}$@BSA was not significantly different, and most [^{64}Cu]CuNC@BSA were

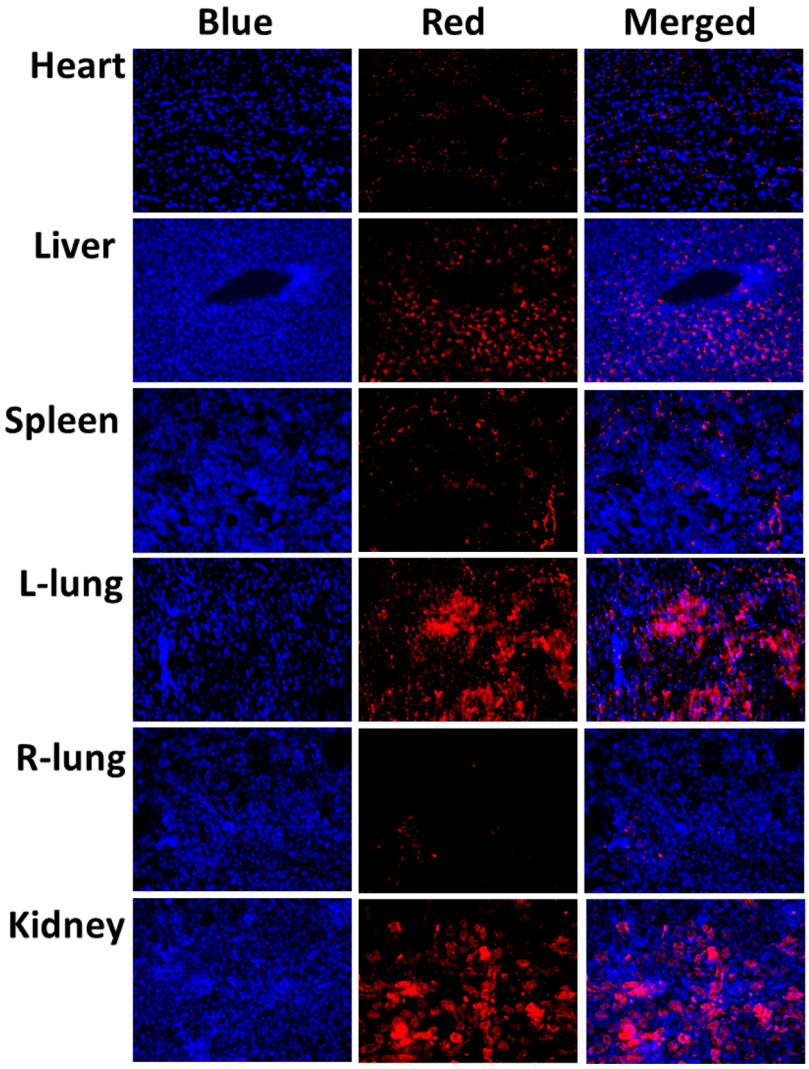

Figure 5. Fluorescent microscopy images of tissue sections. The tissues were taken at 4 h after injection of CF680R-conjugated [^{64}Cu]Cu$_{NC}$@BSA-LHRH *via* tail vein. Blue fluorescence shows nuclei stained with DAPI, and red fluorescence shows the location of [^{64}Cu]Cu$_{NC}$@BSA-LHRH. It showed that [^{64}Cu]CuNC@BSA-LHRH mainly accumulated in left lung inoculated orthotopic A549 tumors and kidney. L-Lung: left lung; R-Lung: right lung.

accumulated in the kidney, followed by the liver and spleen at 4 h postinjection (Figure 6). The tumor selectivity of [^{64}Cu]Cu nanoclusters was further demonstrated by colocalization with tumor marker CD326 (EpCAM) in sequential lung histology slices. Fluorescence microscopy showed that most of the CF680R-conjugated [^{64}Cu]Cu$_{NC}$@BSA-LHRH predominantly accumulated within the tumor (Figure S13, yellow dots), while only a small part of CF680R-conjugated [^{64}Cu]Cu$_{NC}$@BSA located in the tumor. These results were consistent with *in vivo* PET imaging.

DISCUSSION

Lung cancer is a global health problem, representing the leading cause of cancer-related deaths among both men and women.[39] The 5-year survival rates of patients with lung cancer is extremely low (<15%) compared to rates for those with prostate (99%), breast (89%), and colon (64%) cancer.[39] Although there are proven means of early diagnosis available for lung cancer, whether these techniques are effective in terms of improving patient survival or outcome remains unknown.[40] Conventional anatomic imaging techniques such as chest X-ray, computed tomography (CT) scans, bone scans, or magnetic resonance imaging cannot accurately determine the stage of the disease.[41,42] Some invasive examination can lead to pneumothorax and associated morbidity. The PET imaging technique provides highly sensitive and specific data for the diagnosis, staging, and restaging of non-small-cell lung cancer, without the need for a biopsy, and is now well accepted by most physicians as an effective complement to existing imaging modalities.[41,43] At present, [^{18}F]-labeled 2-fluorodeoxyglucose (FDG) is the only PET radiotracer used for routine clinical evaluation, primarily for oncological imaging.[5] Although assessment of tissue metabolism using the tracer FDG provides useful imaging of lung tumors, it is relatively nonspecific and is usually less

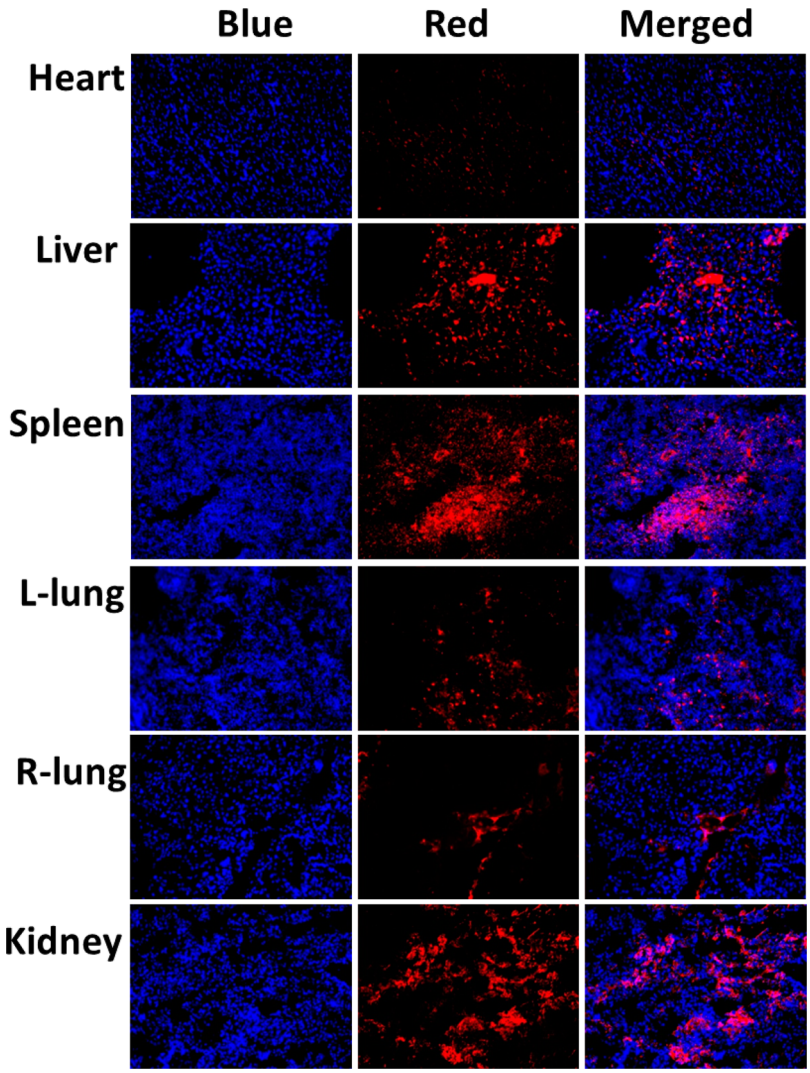

Figure 6. Fluorescent microscopy images of tissue sections. The tissues were taken at 4 h after injection of CF680R-conjugated [^{64}Cu]Cu$_{NC}$@BSA *via* tail vein. Blue fluorescence shows nuclei stained with DAPI, and red fluorescence shows the location of [^{64}Cu]Cu$_{NC}$@BSA. It showed that [^{64}Cu]CuNC@BSA mainly accumulated in the kidney, followed by the liver and spleen.

useful for imaging tumors that have very low growth rates.[1] The development of tracers that target specific molecules is therefore essential for the development and utility of clinically relevant PET procedures. Although many imaging agents have been developed, these agents often demonstrate low specificity, poor accumulation in the target tissue, and slow clearance properties *in vivo*.[14] In this study, we developed chelator-free radioactive [^{64}Cu]Cu nanoclusters as a lung tumor PET imaging agent by using BSA as a scaffold. By conjugating tumor target peptide LHRH to BSA, the prepared ultrasmall [^{64}Cu]Cu$_{NC}$@BSA-LHRH nanoclusters showed high radiolabeling stability, tumor targeting, and rapid renal clearance characteristics. To demonstrate the characteristics of [^{64}Cu]Cu nanoclusters for sensitive and accurate imaging of lung cancer, we mimic localized primary cancer development and its microenvironment using orthotopic lung cancer models. Because orthotopic tumors are located as they would be clinically, orthotopic models are superior to xenografts for imaging evaluation, as they are not situated in areas of artificially low background signal and so better represent clinical presentation.[23] In our current study, orthotopic A549 tumors of the left lung exhibited significantly increased [^{64}Cu]Cu$_{NC}$@BSA-LHRH accumulation compared with the adjacent tissue of the lungs (Figure 4), such as the heart. This is superior to FDG micro-PET images in the same lung tumor model, in which the heart also exhibits intense FDG accumulation.[44] The high-quality images in orthotopic lung cancer models in Figure 4 demonstrate the potential of using [^{64}Cu]Cu nanoclusters in PET imaging. The high resolution and better sensitivity of PET will allow for detection of small and malignant tumors with significantly lower radioactivity dose to the patient compared to SPECT imaging. This is a very important advantage with respect to potential clinical applications. In addition, PET provides noninvasive deep tissue (>5 cm) images, which is not achievable by fluorescence imaging.[1,45] In our current study, although PET and NIRF imaging showed consistent results in the

A549 subcutaneous xenografted tumor model, tumors of the left lung clearly visualized by PET imaging did not show significant fluorescent signal in *in vivo* NIRF imaging in the A549 orthotopic lung tumor model. However, both *ex vivo* NIRF imaging of excised major organs and the biodistribution from average fluorescence signal intensity showed left lung inoculated orthotopic A549 tumors have a significant fluorescent signal after intravenous injection of CF680R-conjugated [^{64}Cu]Cu_{NC}@BSA-LHRH (Figure S12). These results indicated that the limited penetration depth of photons for NIRF imaging hindered noninvasive imaging of deep-seated tumors. Given that most clinical tumors are located in deep positions in the body, PET imaging using [^{64}Cu]Cu nanoclusters as tracers would be more appropriate for translating into the clinical setting.

CONCLUSIONS

In summary, we developed new chelator-free [^{64}Cu]Cu nanoclusters as an efficient radiotracer for PET imaging. By conjugating tumor target peptide LHRH to the BSA shell, the prepared [^{64}Cu]Cu nanoclusters showed high uptake in A549 human lung tumor. In addition, the [^{64}Cu]Cu nanoclusters we developed have many significant advantages, such as high radiolabeling stability, ultrasmall size, rapid deposition and diffusion into the tumor, rapid renal excretion, and predominantly renal clearance. The PET imaging using [^{64}Cu]Cu nanoclusters as tracers showed more sensitive, accurate, and deep penetration imaging of orthotopic lung cancer *in vivo* compared with NIRF imaging. These nanoclusters provide new biomedical research tools for PET molecular imaging.

EXPERIMENTAL METHODS

Materials. Copper(II) chloride ($CuCl_2$), bovine serum albumin, and sodium hydroxide were obtained from Sigma-Aldrich. $^{64}CuCl_2$ was obtained from the China Institute of Atomic Energy. The tiny modified LHRH peptide (Pyr-His-Trp-Ser-Tyr-Gly-Leu-Arg-Pro-Gly-AHx, AHx for 6-aminocaproic acid) was obtained from Wu Han Moon Biosciences Co, Ltd. Deionized water (18 MΩ) was obtained from a Milli-Q synthesis system (Millipore, Billerica, MA, USA).

Synthesis of Cu_{NC}@BSA and Cu_{NC}@BSA-LHRH. $CuCl_2$ (1 mL, 20 mM) and BSA (5 mL, 40 mg/mL) were mixed in water. The solution was stirred at room temperature for 2−3 min, and then 0.4 mL of 0.5 M NaOH was added to adjust the pH to 12, when the color changed from blue to purple. The resulting solution was stirred for 5−6 h at 55 °C. For the synthesis of Cu_{NC}@BSA-LHRH, LHRH was first conjugated to BSA. LHRH peptide (19.5 mg), NHS (1.6 mg), and EDC (10.5 mg) were dissolved in deionized water. The mixture was allowed to react for 30 min in ambient temperature, 100 mg of BSA was added to this solution, and the resulting solution was agitated overnight at ambient temperature. The as-synthesized BSA-LHRH was dialyzed against deionized water for 12 h (dialysis tube MWCO: 12 000), then lyophilized for further use. The amount of LHRH was determined by MALDI-TOF. Cu_{NC}@BSA-LHRH was synthesized as described above except for a BSA-LHRH concentration of 42 mg/mL due to the bioconjugation of LHRH. The synthesized Cu_{NC}@BSA and Cu_{NC}@BSA-LHRH were purified by ultrafiltration (Merck, MWCO: 3000) to remove free ions.

Characterizations of Cu Nanoclusters. For high-resolution transmission electron microscopy, the Cu nanocluster aqueous solution was dropped and dried onto ultrathin carbon-coated copper grids for TEM studies. The HRTEM image was obtained using a JEM-2100 transmission electron microscope (Japan). The ζ-potential, mean size, and size distribution were measured at 25 °C by the DLS technique (NICOMP 380/ZLS (PSS)) and analyzed by ZPW388 software. UV−vis absorption spectra of BSA and Cu nanoclusters were recorded on a Shimadzu UV-1800 spectrophotometer (Japan). Fluorescence spectra of Cu nanoclusters were measured on a Shimadzu RF-5301 fluorescence spectrophotometer (Japan). For MALDI-TOF MS, Cu nanoclusters were tested in the positive ion linear mode. α-Cyano-4-hydroxycinnamic acid was used as the matrix (ABI mass system).

Stability of Cu Nanoclusters. The stabilities of Cu_{NC}@BSA and Cu_{NC}@BSA-LHRH in various media were investigated by incubating Cu_{NC}@BSA and Cu_{NC}@BSA-LHRH in saline, high-glucose DMEM, FBS, and 0.1 mM cysteine solution in pH 7.4 PBS at room temperature for 24 h. For the stabilities of Cu nanoclusters at different pH PBS, Cu_{NC}@BSA and Cu_{NC}@BSA-LHRH were dispersed in pH 7.4 and pH 6.0 PBS, respectively. The appearance of precipitation was observed by visual inspection, and the fluorescence intensity of Cu nanoclusters was detected.

Molecular Simulations for Cu_{NC}@BSA Binding Site and Binding Mode. First, we utilized DFT to obtain the possible isomers of the Cu_5 nanocluster. The calculations were carried out using the GAUSSIAN 09 package. The optimizations of the Cu_5 nanocluster structure were performed by the B3LYP method in conjunction with the SDD pseudopotential basis set. Cu_5-I and Cu_5-II were obtained as the isomers of the Cu_5 nanocluster (shown in Supplementary Figure 5a and b). Second, molecular dynamics simulations were used to find the relaxed conformation of the BSA molecule in solution by the NAMD2.9 package. The crystal structure of BSA (PDB ID: 3V03) was solvated in the TIP3P water model. We neutralized the solvation by adding sodium and chloride ions with a 0.15 M salt concentration as the physiological condition. The CHARMM27 force field was used. The NPT ensemble (T = 310 K, P = 1 atm) was adopted using the Nosé−Hoover Langevin piston method. The particle-mesh Ewald method was utilized for the long-range electrostatic interactions. The smooth cutoff of the short-range electrostatic and van der Waals interactions was set as 12 Å. A time step of 2 fs was used, and the data were collected in steps of 1 ps. We applied periodic boundary conditions in all directions. We adopted the relaxation conformation of BSA after a 15 ns equilibrium run for the molecular docking simulation. Third, we performed molecular docking simulations to find the binding site and binding mode between the Cu_5 nanocluster and BSA molecule with the aid of the AutoDock 4.2 package. All bonds were set as rigid ones. The grid point number of the box was 126 × 126 × 126. A Lamarckian genetic algorithm was used, and the maximum number of generations was set to 2.7×10^4. The docking systems were assigned by adding Kollman charges. There were 1000 docking conformations obtained for Cu_5-I/BSA and Cu_5-II/BSA docking systems, respectively. These docking structures were clustered with an RMSD of less than 2 Å. The results were analyzed by AutoDockTools. Additionally, the VMD package was employed to render the isomers of the Cu_5 nanocluster and snapshots of the Cu_5 nanocluster/BSA binding complex.

Synthesis of Radioactive [^{64}Cu]Cu_{NC}@BSA and [^{64}Cu]Cu_{NC}@BSA-LHRH. The synthesis of [^{64}Cu]Cu_{NC}@BSA and [^{64}Cu]Cu_{NC}@BSA-LHRH followed the same procedure as the preparation of nonradioactive Cu_{NC}@BSA and Cu_{NC}@BSA-LHRH except for the addition of $^{64}CuCl_2$ (555 MBq, 80 μL) to the mixture. The synthesized [^{64}Cu]Cu_{NC}@BSA and [^{64}Cu]Cu_{NC}@BSA-LHRH were purified by following the same procedure as that for nonradioactive Cu_{NC}@BSA and Cu_{NC}@BSA-LHRH.

Radiolabeling Efficiency and Stability. The radiolabeling efficiency and stability of [^{64}Cu]Cu_{NC}@BSA and [^{64}Cu]Cu_{NC}@BSA-LHRH were assessed using radio instant thin layer chromatography

(radio-ITLC). The radio-ITLC strips were developed with PBS (pH 7.4) containing 4 mM EDTA and quantified using a TLC imaging scanner (Bioscan, Washington, DC, USA). The radiolabeling stability was analyzed by incubating [^{64}Cu]Cu_{NC}@BSA and [^{64}Cu]Cu_{NC}@BSA-LHRH in PBS buffer containing 4 mM EDTA or FBS at 37 °C for 24 h. Free $^{64}Cu^{2+}$ ions moved to the solvent front, and the nanocluster remained at the original spot. The radioactivity at the original spot was recorded as a percentage of the total radioactivity of the ITLC strip.

Preparation of CF680R-Conjugated Cu Nanoclusters. A 100 μL amount of CF680R succinimidyl ester was added to the synthesized Cu nanocluster suspension, and the resulting mixture was agitated overnight at 4 °C in the dark. The CF680R bioconjugated Cu nanoclusters were dialyzed against deionized water for 12 h (dialysis tube MWCO: 8000−12 000). The amount of conjugated CF680R was determined by UV/vis spectroscopy measurements at a wavelength of 681 nm.

***In Vitro* Lung Tumor Cells Targeting of Cu Nanoclusters.** Human non-small-cell lung carcinoma A549 cells and noncancerous human embryonic lung fibroblast MRC-5 cells were obtained from the American Type Culture Collection. The A549 cells and MRC-5 cells were respectively maintained in high-glucose DMEM (Hyclone) and minimum essential medium (MEM/EBSS, Hyclone) containing 1 mM sodium pyruvate supplemented with 10% fetal calf serum, 100 U mL^{-1} penicillin, and 100 mg mL^{-1} streptomycin. All cultures were kept in an atmosphere of 5% CO_2 and 95% air at 37 °C. For confocal laser scanning microscope observation, the cells were seeded on glass-bottom dishes (35 mm, MatTek Corporation). After 24 h, 1 mg mL^{-1} of CF680R-conjugated Cu_{NC}@BSA and Cu_{NC}@BSA-LHRH were added to the culture medium. After incubation at 37 °C for 2 h, the cells were washed three times with PBS, fixed with 4% paraformaldehyde, and then stained with 5 μM SYTOX Green (KeyGEN BioTECH) for 10 min. Cells were next washed three times with PBS and were imaged under a Nikon confocal laser scanning microscope (Nikon Ti-e microscope) with excitation at wavelengths of 488 and 640 nm.

For flow cytometry analysis of the cell suspension, cells in the logarithmic growth phase were seeded on six wells at a cell density of 1×10^5 cells mL^{-1}. After 24 h, 1 mg mL^{-1} of CF680R-conjugated Cu_{NC}@BSA and Cu_{NC}@BSA-LHRH were added to the culture medium. After incubation at 37 °C for 2 h, the cells were washed three times with PBS, trypsinized, centrifuged, and resuspended in 400 μL of PBS. Cell suspension was subjected to flow cytometric analysis (BD Accuri C6).

Animal Model. All animal experiments were performed in compliance with the local ethics committee. Female BABL/c athymic nude mice (nu/nu, body weight, around 16 g), 4 weeks of age, were obtained from Beijing HFK Bioscience Co., Ltd., with five mice/cage with water and food *ad libitum* according to Institutional Animal Care and Use Committee approval. For the establishment of the A549 subcutaneous xenografted tumor model, A549 cells (5×10^6 in a mixture of 50 μL of serum-free DMEM media and 50 μL of Matrigel) were injected subcutaneously into the right hind flank of the female BALB/c nude mice. The mice underwent imaging studies when the tumor volume reached 200−500 mm^3 (3−4 weeks after inoculation). For the establishment of the orthotopic A549 lung tumor model, the female BALB/c nude mice were anesthetized by ip injection of 1% sodium pentobarbital (50 mg/kg). The mice were placed in the right lateral decubitus position. The left lateral chest wall was sterilized with iodine followed by 70% alcohol. A 5−10 mm skin incision was made in the left chest at the dorsal midaxillary line just below the inferior border of the scapula (about 1.5 cm above the lower rib line). While monitoring the motion of the left lung, $(1-3) \times 10^6$ cells in a mixture of 12 μL of serum-free DMEM media and 12 μL of Matrigel were injected slowly into the lung parenchyma using a 30 G needle. The incision was closed using nonsilk sutures. The mice were turned to the left lateral decubitus position and kept warm to recover. Two randomly selected mice were killed, and tumor growth was examined at 3−4 weeks after inoculation.

Small-Animal PET Imaging and Biodistribution Studies. Each mouse was injected with about 6.7−7.4 MBq of [^{64}Cu]Cu nanoclusters (0.2 mL) *via* tail vein. The mice bearing subcutaneous or orthotopic A549 lung tumors were anesthetized with 2% isoflurane and placed in the prone position. All PET scans were performed on a small-animal PET scanner (developed by Institute of High Energy Physics, Chinese Academy of Sciences) at indicated time points postinjection. Each scan time was 10 min. At the end point of the experiment, the mice were sacrificed and organs of interest were harvested, weighed, and counted in a gamma counter (CAPRAC-t, Capintec Inc.). The percentage of injected dose per gram (% ID/g) for each sample was calculated by comparing its activity with an appropriate standard of injected dose.

To further confirm the biodistribution of [^{64}Cu]Cu nanoclusters in mice bearing orthotopic A549 lung tumors, CF680R-conjugated [^{64}Cu]Cu_{NC}@BSA and [^{64}Cu]Cu_{NC}@BSA-LHRH were injected into mice *via* tail vein. The mice were sacrificed at 4 h after injection, and some major organs including the heart, liver, spleen, left lung, right lung, and kidneys were dissected and snap-frozen in optimal cutting temperature compound immediately. After the decay of ^{64}Cu, the tissues were cryosectioned at −20 °C into slices of 10 μm thickness, fixed in cold acetone for 5 min, stained with DAPI (Beyotime Institute of Biotechnology) mounting media, and immediately imaged with an Olympus fluorescence microscope (Olympus IXi2-ILL100).

Conflict of Interest: The authors declare no competing financial interest.

Acknowledgment. We acknowledge the financial support of this research by the National Key Basic Research Program of China (2013CB932703), the Natural Science Foundation of China (81472851, 21425522, 31200751, 31300827, 11404333), and Beijing Natural Science Foundation (7152158).

Supporting Information Available: The Supporting Information file contains a HRTEM image and size distribution of Cu_{NC}@BSA-LHRH; the general stability of Cu nanoclusters and the radiolabel stability of [^{64}Cu]Cu nanoclusters; PET images of nude mice bearing subcutaneous A549 xenografted tumors and corresponding organ biodistribution; *in vivo* NIRF optical imaging of A549 subcutaneous xenografted tumor model and A549 orthotopic lung tumor model. The Supporting Information is available free of charge on the ACS Publications website at DOI: 10.1021/nn507130k.

REFERENCES AND NOTES

1. Gambhir, S. S. Molecular Imaging of Cancer with Positron Emission Tomography. *Nat. Rev. Cancer* **2002**, *2*, 683–693.
2. Welch, M. J.; Hawker, C. J.; Wooley, K. L. The Advantages of Nanoparticles for PET. *J. Nucl. Med.* **2009**, *50*, 1743–1746.
3. Cheng, Z. L.; Al Zaki, A.; Hui, J. Z.; Muzykantov, V. R.; Tsourkas, A. Multifunctional Nanoparticles: Cost *versus* Benefit of Adding Targeting and Imaging Capabilities. *Science* **2012**, *338*, 903–910.
4. Rossin, R.; Verkerk, P. R.; van den Bosch, S. M.; Vulders, R. C.; Verel, I.; Lub, J.; Robillard, M. S. *In Vivo* Chemistry for Pretargeted Tumor Imaging in Live Mice. *Angew. Chem., Int. Ed.* **2010**, *49*, 3375–3378.
5. Shokeen, M.; Anderson, C. J. Molecular Imaging of Cancer with Copper-64 Radiopharmaceuticals and Positron Emission Tomography (PET). *Acc. Chem. Res.* **2009**, *42*, 832–841.
6. Schipper, M. L.; Cheng, Z.; Lee, S. W.; Bentolila, L. A.; Iyer, G.; Rao, J. H.; Chen, X. Y.; Wul, A. M.; Weiss, S.; Gambhirl, S. S. MicroPET-Based Biodistribution of Quantum Dots in Living Mice. *J. Nucl. Med.* **2007**, *48*, 1511–1518.
7. Cai, W. B.; Chen, K.; Li, Z. B.; Gambhir, S. S.; Chen, X. Y. Dual-Function Probe for PET and Near-Infrared Fluorescence Imaging of Tumor Vasculature. *J. Nucl. Med.* **2007**, *48*, 1862–1870.
8. Lu, W.; Zhang, G. D.; Zhang, R.; Flores, L. G.; Huang, Q.; Gelovani, J. G.; Li, C. Tumor Site-Specific Silencing of NF-kappa B p65 by Targeted Hollow Gold Nanosphere-Mediated Photothermal Transfection. *Cancer Res.* **2010**, *70*, 3177–3188.
9. Zhang, G. D.; Yang, Z.; Lu, W.; Zhang, R.; Huang, Q.; Tian, M.; Li, L.; Liang, D.; Li, C. Influence of Anchoring Ligands and Particle Size on the Colloidal Stability and *in Vivo*

Biodistribution of Polyethylene Glycol-Coated Gold Nanoparticles in Tumor-Xenografted Mice. *Biomaterials* **2009**, *30*, 1928–1936.
10. Liu, Z.; Cai, W. B.; He, L. N.; Nakayama, N.; Chen, K.; Sun, X. M.; Chen, X. Y.; Dai, H. J. *In Vivo* Biodistribution and Highly Efficient Tumour Targeting of Carbon Nanotubes in Mice. *Nat. Nanotechnol.* **2007**, *2*, 47–52.
11. Schluep, T.; Hwang, J.; Hildebrandt, I. J.; Czernin, J.; Choi, C. H. J.; Alabi, C. A.; Mack, B. C.; Davis, M. E. Pharmacokinetics and Tumor Dynamics of the Nanoparticle IT-101 from PET Imaging and Tumor Histological Measurements. *Proc. Natl. Acad. Sci. U.S.A.* **2009**, *106*, 11394–11399.
12. Yang, Z.; Zheng, S. Y.; Harrison, W. J.; Harder, J.; Wen, X. X.; Gelovani, J. G.; Qiao, A.; Li, C. Long-Circulating Near-Infrared Fluorescence Core-Cross-Linked Polymeric Micelles: Synthesis, Characterization, and Dual Nuclear/Optical Imaging. *Biomacromolecules* **2007**, *8*, 3422–3428.
13. Pressly, E. D.; Rossin, R.; Hagooly, A.; Fukukawa, K. I.; Messmore, B. W.; Welch, M. J.; Wooley, K. L.; Lamm, M. S.; Hule, R. A.; Pochan, D. J.; *et al*. Structural Effects on the Biodistribution and Positron Emission Tomography (PET) Imaging of Well-Defined Cu-64-Labeled Nanoparticles Comprised of Amphiphilic Block Graft Copolymers. *Biomacromolecules* **2007**, *8*, 3126–3134.
14. Wadas, T. J.; Anderson, C. J. Radiolabeling of TETA- and CB-TE2A-Conjugated Peptides with Copper-64. *Nat. Protoc.* **2006**, *1*, 3062–3068.
15. Wadas, T. J.; Wong, E. H.; Weisman, G. R.; Anderson, C. J. Coordinating Radiometals of Copper, Gallium, Indium, Yttrium, and Zirconium for PET and SPECT Imaging of Disease. *Chem. Rev.* **2010**, *110*, 2858–2902.
16. Cutler, C. S.; Hennkens, H. M.; Sisay, N.; Huclier-Markai, S.; Jurisson, S. S. Radiometals for Combined Imaging and Therapy. *Chem. Rev.* **2013**, *113*, 858–883.
17. Sanhai, W. R.; Sakamoto, J. H.; Canady, R.; Ferrari, M. Seven Challenges for Nanomedicine. *Nat. Nanotechnol.* **2008**, *3*, 242–244.
18. Bass, L. A.; Wang, M.; Welch, M. J.; Anderson, C. J. *In Vivo* Transchelation of Copper-64 from TETA-Octreotide to Superoxide Dismutase in Rat Liver. *Bioconjugate Chem.* **2000**, *11*, 527–532.
19. Boswell, C. A.; Sun, X. K.; Niu, W. J.; Weisman, G. R.; Wong, E. H.; Rheingold, A. L.; Anderson, C. J. Comparative *in Vivo* Stability of Copper-64-Labeled Cross-Bridged and Conventional Tetraazamacrocyclic Complexes. *J. Med. Chem.* **2004**, *47*, 1465–1474.
20. Wang, Y. C.; Liu, Y. J.; Luehmann, H.; Xia, X. H.; Brown, P.; Jarreau, C.; Welch, M.; Xia, Y. N. Evaluating the Pharmacokinetics and *in Vivo* Cancer Targeting Capability of Au Nanocages by Positron Emission Tomography Imaging. *ACS Nano* **2012**, *6*, 5880–5888.
21. Petersen, A. L.; Binderup, T.; Rasmussen, P.; Henriksen, J. R.; Elema, D. R.; Kjaer, A.; Andresen, T. L. Cu-64 Loaded Liposomes as Positron Emission Tomography Imaging Agents. *Biomaterials* **2011**, *32*, 2334–2341.
22. Liu, T. W.; MacDonald, T. D.; Shi, J. Y.; Wilson, B. C.; Zheng, G. Intrinsically Copper-64-Labeled Organic Nanoparticles as Radiotracers. *Angew. Chem., Int. Ed.* **2012**, *51*, 13128–13131.
23. Liu, T. W.; MacDonald, T. D.; Jin, C. S.; Gold, J. M.; Bristow, R. G.; Wilson, B. C.; Zheng, G. Inherently Multimodal Nanoparticle-Driven Tracking and Real-Time Delineation of Orthotopic Prostate Tumors and Micrometastases. *ACS Nano* **2013**, *7*, 4221–4232.
24. Sun, X. L.; Huang, X. L.; Yan, X. F.; Wang, Y.; Guo, J. X.; Jacobson, O.; Liu, D. B.; Szajek, L. P.; Zhu, W. L.; Niu, G.; *et al*. Chelator-Free Cu-64-Integrated Gold Nanomaterials for Positron Emission Tomography Imaging Guided Photothermal Cancer Therapy. *ACS Nano* **2014**, *8*, 8438–8446.
25. Zhou, M.; Zhang, R.; Huang, M. A.; Lu, W.; Song, S. L.; Melancon, M. P.; Tian, M.; Liang, D.; Li, C. A Chelator-Free Multifunctional [Cu-64]CuS Nanoparticle Platform for Simultaneous Micro-PET/CT Imaging and Photothermal Ablation Therapy. *J. Am. Chem. Soc.* **2010**, *132*, 15351–15358.
26. Zhao, Y. F.; Sultan, D.; Detering, L.; Cho, S. H.; Sun, G. R.; Pierce, R.; Wooley, K. L.; Liu, Y. J. Copper-64-Alloyed Gold Nanoparticles for Cancer Imaging: Improved Radiolabel Stability and Diagnostic Accuracy. *Angew. Chem., Int. Ed.* **2014**, *53*, 156–159.
27. Kim, B. H.; Hackett, M. J.; Park, J.; Hyeon, T. Synthesis, Characterization, and Application of Ultrasmall Nanoparticles. *Chem. Mater.* **2014**, *26*, 59–71.
28. Kharissova, O. V.; Kharisov, B. I.; Jimenez-Perez, V. M.; Flores, B. M.; Mendez, U. O. Ultrasmall Particles and Nanocomposites: State of the Art. *RSC Adv.* **2013**, *3*, 22648–22682.
29. Zhang, X. D.; Luo, Z. T.; Chen, J.; Shen, X.; Song, S. S.; Sun, Y. M.; Fan, S. J.; Fan, F. Y.; Leong, D. T.; Xie, J. P. Ultrasmall Au10-12(SG)(10-12) Nanomolecules for High Tumor Specificity and Cancer Radiotherapy. *Adv. Mater.* **2014**, *26*, 4565–4568.
30. Dharap, S. S.; Wang, Y.; Chandna, P.; Khandare, J. J.; Qiu, B.; Gunaseelan, S.; Sinko, P. J.; Stein, S.; Farmanfarmaian, A.; Minko, T. Tumor-Specific Targeting of an Anticancer Drug Delivery System by LHRH Peptide. *Proc. Natl. Acad. Sci. U.S.A.* **2005**, *102*, 12962–12967.
31. Taratula, O.; Garbuzenko, O. B.; Kirkpatrick, P.; Pandya, I.; Savla, R.; Pozharov, V. P.; He, H. X.; Minko, T. Surface-Engineered Targeted PPI Dendrimer for Efficient Intracellular and Intratumoral siRNA Delivery. *J. Controlled Release* **2009**, *140*, 284–293.
32. Taheri, A.; Dinarvand, R.; Ahadi, F.; Khorramizadeh, M. R.; Atyabi, F. The *in Vivo* Antitumor Activity of LHRH Targeted Methotrexate-Human Serum Albumin Nanoparticles in 4T1 Tumor-Bearing Balb/c Mice. *Int. J. Pharm.* **2012**, *431*, 183–189.
33. Mathew, A.; Sajanlal, P. R.; Pradeep, T. A Fifteen Atom Silver Cluster Confined in Bovine Serum Albumin. *J. Mater. Chem.* **2011**, *21*, 11205–11212.
34. Guvelioglu, G. H.; Ma, P. P.; He, X. Y.; Forrey, R. C.; Cheng, H. S. First Principles Studies on the Growth of Small Cu Clusters and the Dissociative Chemisorption of H-2. *Phys. Rev. B* **2006**, 155436 (1−10).
35. Gong, H. F.; Li, G. P.; Jia, Y. H. Isomers of the Cu-5 Cluster: A Density Function Theory Study. *Chin. Phys. B* **2011**, 033105 (1−6).
36. Lin, X.; Xie, J.; Niu, G.; Zhang, F.; Gao, H.; Yang, M.; Quan, Q.; Aronova, M. A.; Zhang, G.; Lee, S.; *et al*. Chimeric Ferritin Nanocages for Multiple Function Loading and Multimodal Imaging. *Nano Lett.* **2011**, *11*, 814–819.
37. Yang, X. D.; Ma, J. K. A.; Malanga, C. J.; Rojanasakul, Y. Characterization of Proteolytic Activities of Pulmonary Alveolar Epithelium. *Int. J. Pharm.* **2000**, *195*, 93–101.
38. McDonald, D. M.; Baluk, P. Significance of Blood Vessel Leakiness in Cancer. *Cancer Res.* **2002**, *62*, 5381–5385.
39. Siegel, R.; Naishadham, D.; Jemal, A. Cancer Statistics, 2013. *Ca-Cancer J. Clin.* **2013**, *63*, 11–30.
40. Etzioni, R.; Urban, N.; Ramsey, S.; McIntosh, M.; Schwartz, S.; Reid, B.; Radich, J.; Anderson, G.; Hartwell, L. The Case for Early Detection. *Nat. Rev. Cancer* **2003**, *3*, 243–252.
41. Chen, X. Y.; Sievers, E.; Hou, Y. P.; Park, R.; Tohme, M.; Bart, R.; Bremner, R.; Bading, J. R.; Conti, P. S. Integrin Alpha(V)Beta-(3)-Targeted Imaging of Lung Cancer. *Neoplasia* **2005**, *7*, 271–279.
42. Jokerst, J. V.; Lobovkina, T.; Zare, R. N.; Gambhir, S. S. Nanoparticle PEGylation for Imaging and Therapy. *Nanomedicine* **2011**, *6*, 715–728.
43. Shankar, L. K.; Sullivan, D. C. Functional Imaging in Lung Cancer. *J. Clin. Oncol.* **2005**, *23*, 3203–3211.
44. Graves, E. E.; Vilalta, M.; Cecic, I. K.; Erler, J. T.; Tran, P. T.; Felsher, D.; Sayles, L.; Sweet-Cordero, A.; Le, Q. T.; Giaccia, A. J. Hypoxia in Models of Lung Cancer: Implications for Targeted Therapeutics. *Clin. Cancer Res.* **2010**, *16*, 4843–4852.
45. Ntziachristos, V.; Ripoll, J.; Wang, L. H. V.; Weissleder, R. Looking and Listening to Light: The Evolution of Whole-Body Photonic Imaging. *Nat. Biotechnol.* **2005**, *23*, 313–320.